IEEE Access
Multidisciplinary | Rapid Review | Open Access Journal

Received 29 March 2024, accepted 9 April 2024, date of publication 11 April 2024, date of current version 22 April 2024.

Digital Object Identifier 10.1109/ACCESS.2024.3387872

RESEARCH ARTICLE

Investigating the Influence of Free-Electron Pulses and Neutral Excited Species Formation on Discharge Development: By PD Quantum Optics Analysis and Plasma Simulation

YUNING FENG[1], ZHIYUAN CAI[1], SHUN YUAN[1,2], SHAOHUA MA[1], AND ENLIANG HUI[1]
[1]Key Laboratory of Special Machine and High Voltage Apparatus, Ministry of Education, Shenyang University of Technology, Shenyang, Liaoning 110870, China
[2]National Energy Administration, Beijing 100031, China

Corresponding author: Yuning Feng (13291149113@163.com)

ABSTRACT Previous studies on discharge dynamics have primarily focused on the generation and migration of the charged particles and neglecting the influence of neutral excited-state particles. In this study, an integrated approach combining experiment and simulation was used to investigate the effect of neutral excited particles on discharge development. Firstly, partial discharge was induced by applying voltage to a pin-plate electrode in a darkroom environment and the emission spectrum of discharge was captured using an ultra-sensitive spectrometer. Then the formation mechanism of the main neutral excited particles in air corona discharge was analyzed based on the principle of quantum optics, and the collision cross-section data of the non-local thermodynamic equilibrium (NLTE) plasma chemical model for air was updated accordingly. Simulations revealed the process of electron pulses initiates the electron avalanche, which leads to dielectric breakdown. Results indicated that overvoltage can lead to the formation of electron avalanches at defect sites, which is capable of causing dielectric breakdown within the nanosecond time scale. The competitive mechanism of the excitation reactions to ionization reactions results in the dissipation of free electrons' energy, effectively suppressing the development of electron avalanches and preventing electrical breakdown.

INDEX TERMS High-voltage techniques, insulation, gas discharges, quantum optics, low-temperature plasmas, plasma transport processes, plasma chemistry, plasma simulation applications.

I. INTRODUCTION

In the domain of high-voltage equipment, the quality of insulation is imperative. The perils engendered by partial discharge (PD) are substantial, as it precipitates long-term material degradation which may culminate in catastrophic failures [1], [2], [3], [4], [5]. In order to fortify the insulation systems, academicians and industry experts have embarked on comprehensive research initiatives. These initiatives include the deployment of a spectrum of detection technologies for the precursory identification of incipient faults attributable to partial discharges [6], [7], [8], [9], alongside the refinement of insulation design facilitated by a deeper understanding of partial discharge development mechanisms [10], [11]. However, the heterogeneity and unpredictability of defect typologies, spatial distribution, and dimensional extents introduce additional complexities to these investigative pursuits [12]. The diverse expanse of operating parameters and associated mechanisms obfuscates the formulation of a unified scaling law for electron emission and gas breakdown [13]. A thorough investigation of PD mechanisms is imperative for two reasons: one is to refine theoretical models for PD detection and the other is to diminish PD's detrimental effects through advanced technology. Conventional experimental techniques face challenges in fully capturing PD intricacies. Spectroscopic techniques,

The associate editor coordinating the review of this manuscript and approving it for publication was Jenny Mahoney.

© 2024 The Authors. This work is licensed under a Creative Commons Attribution 4.0 License.
For more information, see https://creativecommons.org/licenses/by/4.0/

which are non-invasive, highly noise-resistant, and probe intrinsic properties, are vital for assessing electrical insulation integrity and identifying potential system failures proactively [14], [15], [16]. Recent studies have proved the effectiveness of spectroscopy in visualizing and analyzing partial discharge (PD) phenomena in various electrical systems [17], [18], [19]. Ultra-sensitive multispectral PD optical sensors have been designed and demonstrated to be capable of sensitive detection of early partial discharge defects [20]. High-fidelity numerical simulations provide insights beyond the scope of macroscopic studies, progress in simulation technology has significantly advanced our understanding and management of PD, though opportunities for further methodological precision remain.

At the dawn of the 20th century, Thomson's theories on electrical discharge laid the foundational understanding for insulation material breakdown. In recent years, researchers have employed finite element analysis based on theoretical frameworks to account for the impact of charged particles on electric fields, as well as their redistribution during discharge events. This advanced model has led to a more accurate prediction of local discharge, providing a more robust scientific basis for the design, diagnostics, and estimation of lifespan of high-voltage equipment [21], [22], [23], [24], [25], [26]. Although computationally less demanding, these methods struggle to capture the complex dynamics of discharges. As electrical systems have grown in complexity, the limitations of simulation models based solely on electric field intensity have become increasingly evident, particularly in representing the dynamic behavior of carriers in nonlinear media. To address this, scholars have integrated the Drift-Diffusion Model (DDM) with multiphysics fields, combining fluid dynamics and electromagnetic calculations to create a simplified plasma dynamics model. This approach has significantly improved the accuracy of discharge behavior predictions in electrical insulation systems when applied to the analysis of discharges.

The field has seen significant advancements as experts have expanded the scope of these models to encompass more complex particle dynamics, moving from single-species to multi-species particle systems. This expansion has led to a more profound understanding of charged particle behavior [27], [28], [29], [30]. These models have been utilized to study the effects of ion winds and airflow in corona discharge [31], [32], [33], to analyze the influence of discharge parameters and pulse characteristics [34], [35], and to scale up to practical engineering applications [36]. They've also been pivotal in examining the impact of corona discharge on the potential decay on the surfaces of nanocomposite materials [37]. Technological advancements have led to continuous improvements and validations of these models, enhancing both computational efficiency and applicability, as well as the precision with which they handle complex data, thereby deepening our understanding of discharge phenomena. Improved models based on DDM have revealed the principles behind discharge trees [38], [39], [40], [41], [42], and pulse discharges and have enhanced the accuracy of predictions regarding low-temperature plasma interactions with various materials [41], [43], [44], [45], [46], [47]. By integrating fluid dynamics models with ion transport equations upon the Kaptzov hypothesis, the analytical ability of the model is improved and has achieved numerical simulation of the charged particle distribution produced by corona discharge from a needle electrode over large spatial scales [48].

Traditional DDM frameworks, which overlook collision cross-sections in plasma, are inadequate for simulating the detailed chemical reactions caused by localized discharges. The generation of active species, discharge pathways, and the distribution of energy on micro and mesoscales are crucial in guiding the directed evolution of discharge paths. These elements are essential for the insulation performance and life expectancy of electrical apparatuses. Accurate chemical reaction data is critical for deeper understanding of how these processes might influence the overall insulation structure and performance of devices. Moreover, advancements in the precise control and monitoring of plasma parameters are crucial for enhancing the performance of electrical devices. Integrating energy-dependent collision cross-sections into plasma models based on DDM are essential for accurate simulations of discharge phenomena.

Researchers at the Budapest University of Technology and Economics conducted a comparative study of complex plasma chemical models which include collision cross-section parameters against their simplified counterparts, excluding plasma chemistry. Their findings underscore the critical importance and superiority of utilizing detailed plasma chemical models for accurately simulating corona discharge events [49]. Plasma chemical models have already provided in-depth insights into the mechanisms of localized discharges, fostering improvements in high-voltage cable insulation, pollution control, and surface treatment technologies. These advancements have affirmed the scientific and practical value of the plasma chemical models that consider collision cross-section data [50], [51], [52], [53], [54].

It is evident that collision cross-section data is indispensable for unraveling chemical reaction mechanisms and finely tuning plasma processes, especially when dealing with collision-dominated chemical reaction kinetics. Interactions among particles are parameterized through these collision cross-sections, which are critical for understanding and predicting energy and matter transfers within the plasma. In the efforts to create models that can converge to stable solutions within the limits of computational resources, prior researchers have often focused on the collision processes of charged particles while neglecting the effect of the formation process of neutral excited species on discharge dynamics. However, the influence of these species on the overall behavior of plasma is extremely important, particularly in the analysis of breakdown mechanisms and electron avalanche phenomena. Although these particles do not directly respond to electric fields, they can still alter the energy distribution

of electrons via inelastic collision processes, affecting the initiation and progress of electron avalanches, and significantly impacting the dielectric breakdown characteristics of the plasma [55].

Simulation by plasma chemical model can be a daunting task, even merely modeling the ionization processes is a vast undertaking, and this complexity is further increased when excited-state reactions are included. Attempting to incorporate all possible excited states and neutral particle reactions not only leads to significant consumption of computational resources but also complicates the model, making it difficult to parse and optimize. Contact-based detection methods for these rapid chemical reactions is highly challenging, as the high-intensity electric field environment within the discharge region can interfere with contact-based detection methods, potentially disturbing the discharge itself and leading to inaccurate data. Therefore, by analyzing the spectrum emitted from the plasma, diagnose specific spectral lines associated with key excited-state reactions in a non-invasive manner. Is an exceptionally effective method for identifying the key reactions in the progression of PD.

In this study, a plasma chemistry model was used to simulate the evolution of partial discharge cold plasma with the formation of a neutral excited state incorporated. Spectroscopic detection methods were utilized to diagnose specific types of reactions within the plasma. By accurately measuring and analyzing the spectral lines emitted from the plasma, key excited-state reactions that influence plasma behavior are identified and quantified, providing empirical support for the construction and optimization of plasma models.

By analyzing the chemical reactions in PD plasmas, the study not only provides theoretical guidance for optimizing electrical appliance design to avoid PD damage but also provides key data for plasma processes. Furthermore, an in-depth understanding of plasma properties and behavior can also provide data support for plasma technology applications in many fields, such as environmental remediation, material processing, and energy efficiency.

II. PARTIAL DISCHARGE EXPERIMENTS AND SPECTRAL SIGNAL DETECTION AND ANALYSIS

A. EXPERIMENTAL METHODS AND KEY EQUIPMENT

The schematic of the experiment is detailed in Figure 1.

The transformer, capable of handling peak voltages up to 100 kV at a frequency of 50 Hz, facilitated the precise adjustment of the alternating current input voltage to the levels necessitated by the experiment. It incorporated a fine-tuning control mechanism for voltage modulation and a digital display for real-time voltage monitoring, ensuring accurate application of the specified AC voltage peaks to the discharge process.

Two water resistors, with a nominal resistance of 110 kΩ, were integrated into the circuit primarily as a safety mechanism to limit the current surge associated with a specimen

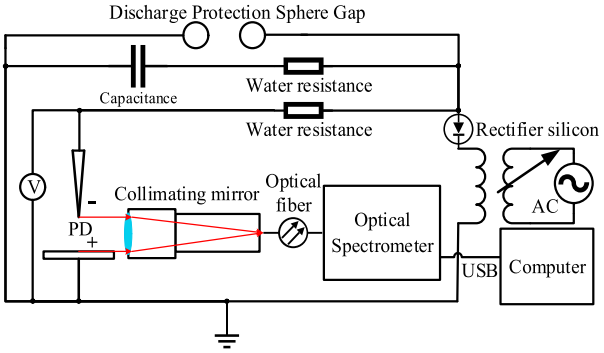

FIGURE 1. Simplified schematic of the partial discharge detection.

breakdown, thus protecting the circuit from the resultant transient spikes that could compromise the experimental setup. The resistor's high resistance value and thermal dissipation properties were critical for mitigating the thermal effects induced by high-voltage operations.

In the circuit, the rectifying silicon stack, rated for a maximum voltage of 180 kV and a current of 0.5 A, the function of the rectifying silicon stack is to filter out the positive half-waves of the alternating current. After the rectifying silicon stack removes the reverse voltage from the transformer, the circuit's capacitors are charged via a water resistor. This method converts the AC voltage into a DC voltage of negative polarity that matches its peak value, which is then applied across the test specimen.

The voltage-regulating capacitor, featuring a capacitance of 2000 μF and a voltage rating of 50 kV, collaborates with the previously mentioned rectifying silicon stack and acts to smooth out the rectified voltage, stabilizing the voltage and providing a DC output.

The discharge protection sphere gap serves as a safeguard in the circuit, which is designed to prevent voltage surges from exceeding the maximum tolerances of the equipment. The sphere gap distance can be finely tuned to ensure that its breakdown voltage aligns, which in this study is set to −50 kV DC, with the capacitor's maximum voltage rating. When the voltage surpasses the equipment's safe operating thresholds, this adjustable device protects the equipment by discharging to dissipate energy.

This configuration ensures that the AC is effectively inverted into a DC voltage with the desired polarity for application across the test specimen.

To acquire accurate and interference-free spectral data of partial discharge emissions, the experiments were meticulously designed to generate partial discharge in a quiet, dark environment devoid of ambient light. Moreover, the indoor temperature was maintained near 0 °C to ensure the effective operation of the infrared temperature measurement device. In the experimental setup, the emitted spectra from the discharge region were captured by using a Wyoptics 94UV type convex collimating lens with an effective diameter of 30 mm, which was utilized to collect and direct the light

emitted from the discharge event into an optical fiber to a spectrometer for analysis.

The discharge experiments utilized a needle-shaped electrode made from C28000 copper-zinc alloy, with a diameter of 3 mm and length of 25 mm, ending in a finely machined tip with a radius of 0.1 mm. This configuration was designed to concentrate the electric field, reduce the threshold voltage for discharge initiation, and enhance the safety and efficiency of the system. The counter electrode, a plate with smooth rounded edges, was positioned at a fixed distance of 12 mm from the needle. The details of the electrodes are as shown in Figure 2.

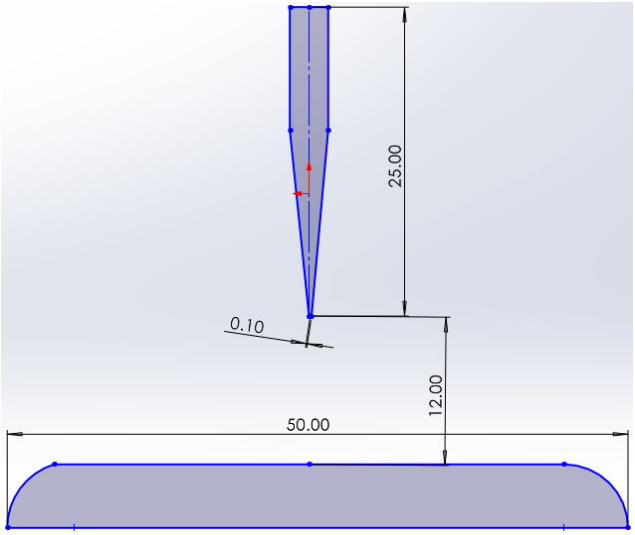

FIGURE 2. Discharge electrode structure.

Figure 3 shows the key optical signal acquisition equipments used in the study. As shown in Figure 3 (A), the imaging system used for the experiment is from the Luminar series developed by OFIL in Israel. It provides an advanced detection capability, enabling the capture of significantly brightened images from the inherently weak light emissions generated by partial discharges.

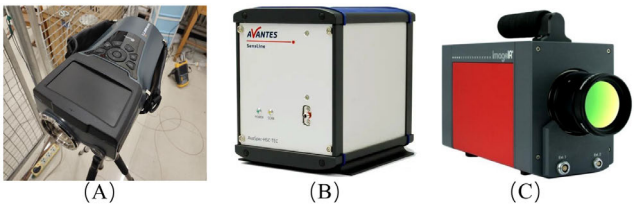

FIGURE 3. Key optical signal acquisition equipment.

As shown in Fig. 3 (B), The discharge spectra were collected using the AvaSpec-HERO series ultra-high sensitivity spectrometer. This spectrometer has a wavelength range of 185-1100 nm and a resolution of 1.8nm. It is characterized by its high sensitivity, allowing for the detection of low-intensity light signals.

As shown in Fig. 3 (C), to monitor the plasma temperature after discharge, the INFRATEC infrared imager was used to photograph the infrared impact caused by the discharge. The imager can cooperate with IRBIS infrared thermal image processing software to accurately detect the temperature of the discharge area.

The experimental procedure involved a step-up voltage method, starting with an initial voltage of −1 kV and increasing it by −1 kV increments until breakdown occurred. At each incremental peak voltage level, the discharge was sustained for 300 seconds to ensure steady-state conditions. The corresponding spectral and imaging data under each applied voltage were recorded under repeated experiments.

The Luminar series imaging system, capable of ultraviolet-visible light intensification, was employed to record the discharge events in a video format, thus facilitating real-time observation. This imaging modality was selected to elucidate the spatial distribution and temporal consistency of the electrical discharges.

The spectrometer was set up to acquire spectral data with an integration time of 1 s per measurement. To ensure the accuracy of the spectral data and reduce the impact of random noise, each data point reported was an average of 10 measurements.

Before data collection, the spectrometer was subjected to a basic calibration procedure to ensure the fidelity of the spectral output to actual spectral characteristics.

Although the experimental environment of the darkroom avoids the interference of ambient light on the data, the background noise caused by the electromagnetic field interference and the equipment's dark current is still a non-negligible influence factor. Avantes spectrometers come equipped with software that can filter out background noise. Before each experiment, background noise can be recorded and filtered out using this software. In this study, the background noise has been recorded and eliminated before each measurement.

B. EVALUATION AND OPTIMIZATION MEASURES OF FACTORS AFFECTINT THE ACCURACY OF THE DETECTION SYSTEM

The current investigation entailed the quantification of optical emissions spectra data resulting from partial discharges, which are intrinsically faint. The identification and reduction of potential error sources are crucial for ensuring the precision and reliability of experimental findings. Potential experimental errors may arise from dark noise inherent to the detection equipment, insufficient resolution, and ambient light interference. To mitigate these errors and enhance signal detection, the following measures were implemented:

1. Selective use a high-sensitivity spectrometer for capturing optical signals emitted during partial discharge events. Although the use of such spectrometers can slightly reduce resolution, this trade-off is deemed acceptable within the context of this study. Optical signals from partial discharges typically manifest as clear, discrete spectral lines that do not require high resolution for discernment. The elevation

in instrument sensitivity assumes greater importance for the detection of these weak signals;

2. Comprehensive calibration of the spectrometer before the commencement of experiments was performed to ensure the accuracy of spectral line data;

3. To attenuate thermal noise and enhance signal detection fidelity, the laboratory environment was conditioned to maintain the ambient temperature marginally above the freezing point. This measure ensured the thermal noise was minimized without risking condensation, which could potentially compromise the integrity of the spectrometer. Moreover, the spectral measurements were performed in a darkroom environment with stringent light control in order to against data corruption due to ambient light;

4. Repeated measurements the emission spectral data with subsequent averaging to ascertain the accuracy and reliability of the spectral data;

5. Calibration of the collimating lens's direction and scope was carried out pre-experiment to ensure the encompassment of the discharge area within the effective collection range.

C. ANALYSIS OF EXPERIMENTAL RESULTS

The corresponding spectral and imaging data under each applied voltage are shown in Figure 4. Given the discharge's weak visibility, amplified optical images were captured using a light-enhancing imager. The images indicate that the needle-plate electrode sustained a corona discharge state at −5 kV. However, a gap breakdown was observed when the voltage increased to −6 kV.

FIGURE 4. Discharge enhanced optical image.

Figure 5 presents an infrared image during a −6 kV discharge, showing that the peak plasma temperature post-discharge was below 18 °C. This is attributed to a water resistor in the circuit, which significantly restricted current post-dielectric breakdown. During the discharge process, the limited increase in current results in a negligible temperature rise in the discharge area, hence peak temperatures remained under 18 °C. Given that significant currents leading to corresponding temperature increases are not present in short-gap partial discharges before complete breakdown, NLTE plasma simulations are appropriate for modeling these pre-breakdown processes.

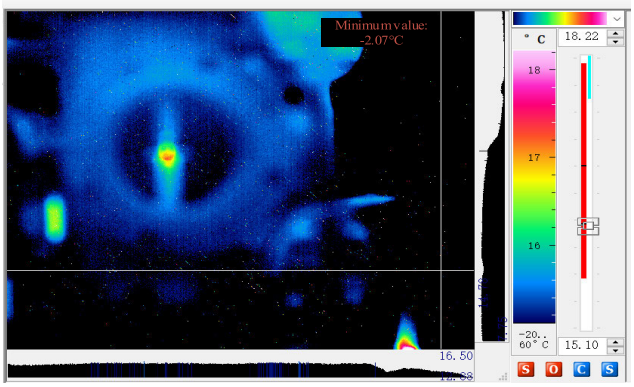

FIGURE 5. Discharge infrared image under the applied voltage of −6 kV.

This study focuses primarily on the breakdown process. Therefore, the spectral data for discharge were collected at an applied pre-breakdown voltage of −5 kV, the spectral measurements were performed by setting the spectrometer integration time to 1 s, with multiple readings taken. The collected discharge spectra data were consistently similar across these measurements, as shown in the following Figure 6 and Figure 7.

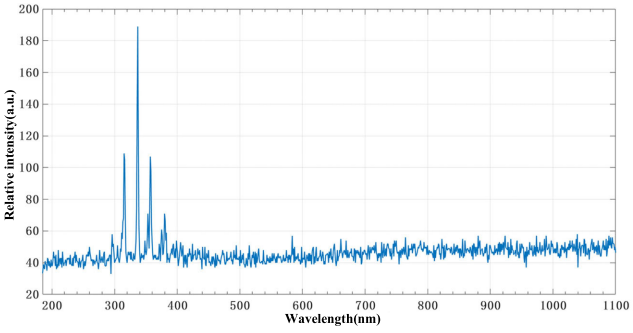

FIGURE 6. Corona discharge emission spectrum in the 185-1100 nm range under the applied voltage of −5 kV.

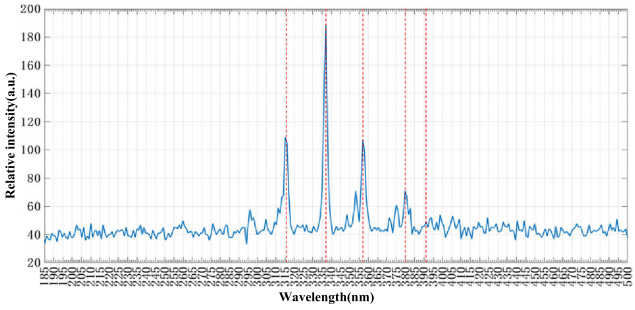

FIGURE 7. Corona discharge emission spectrum in the 185-500 nm range under the applied voltage of −5 kV.

During the experiment, it was observed that when the applied voltage exceeded to −5 kV, electrical breakdown occurred, and below this voltage threshold, the system remained in a state of corona discharge. Spectral line

distributions during this corona discharge phase were similar. The transition phase between PD and BD occurs between −5 kV and −6 kV.

To study the evolution from corona discharge to electrical breakdown, analyzing the spectral lines at −5 kV is beneficial. This is because −5 kV provides a snapshot of the spectral features of a stable partial discharge, which is close to the breakdown voltage. Analyzing these spectral lines can give insights into the precursory phenomena leading up to the breakdown, and help identify the specific conditions under which the stable corona discharge begins to transition into an unstable electrical breakdown state.

The research identified specific spectral lines through the observation and analysis of spectrograms. These lines mainly correspond to the electronic transitions of nitrogen molecules (N_2) from the $C^3\Pi_u$ (an excited state) to the $B^3\Pi_g$ (another excited state), which are characteristic lines of the second positive system of N_2 molecules [56], as shown in the following figure 8:

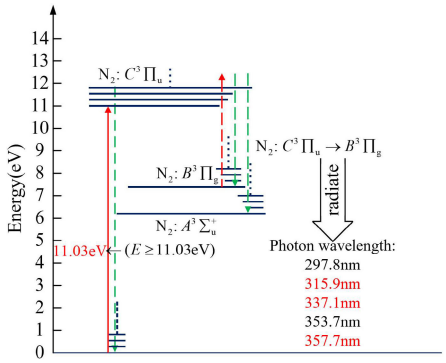

FIGURE 8. Energy transitions of N_2 first positive system.

During the corona phase of PD, the discharge process is dominated by non-equilibrium electron collision excitation rather than thermal ionization. Thus, the excitation of N2 molecules from the ground state $X^1\Sigma_g^+$ to the excited state $C^3\Pi_u$ energy level is primarily induced by collisions. At the initial stages of partial discharge, when electron density is low, the probability of non-radiative transitions for N2 in the $C^3\Pi_u$ excited state is minimal, and de-excitation primarily occurs through spontaneous radiation. As reported in the study by Valk [57], the average lifetime of the N2 $C^3\Pi_u$ excited state is about 41.9ns. Although this timescale is relatively brief, the ionization of the N2 $C^3\Pi_u$ state has a limited impact on the development of the discharge. This is mainly because, although these excited neutral molecules may de-excite to other excited states and emit photons, the energy of these photons is typically below the ionization potential of nitrogen and oxygen molecules. Moreover, any high-energy level photons with wavelengths nearing or shorter than 100 nm are rapidly absorbed by gas molecules within picoseconds. In addition, due to the relatively weak intensity of corona discharge, the number of photons generated from such excited states is limited. Therefore, in the simulation of the partial discharge process, the influence of de-excitation from the N2 $C^3\Pi_u$ state on the development of the discharge is neglected.

Through spectral analysis and the study of quantum chemical reactions, a deeper understanding of the electronic state transitions of N_2 molecules during the discharge process, especially the formation of the $C^3\Pi_u$ state, has been achieved. This will provide theoretical support for the revision of collision cross-section data in simulation models.

III. PLASMA SIMULATION STUDY

A. SIMULATION MODEL DETAILS AND PARAMETER ADJUSTMENT

Based on the observations from the needle-plate electrode discharge experiments previously discussed, this study has opted to employ an NLTE plasma dynamics model that incorporates chemical reactions. The model employed in this study captures the dynamic behavior of plasma by coupling three fundamental components: the evolution of the electric field, particle transport mechanisms, and the reaction cross-sections that dictate the rates of various chemical processes.

1) ELECTRIC FIELD

In the calculation of the electrostatic field, the presence of space charge significantly influences the electric field distribution. Additionally, the charged particles produced by the plasma reaction impact the allocation of space charge. Hence, the computation of the electrostatic field necessitates the resolution of the electric field under the charge and charged particle influence via the Poisson equation. The charge is then determined by calculating the number density of electrons and other charged particles. Equations (1) and (2) describe the computation process of the electrostatic field:

$$-\nabla\cdot\varepsilon_0\varepsilon_r\nabla V=\rho \tag{1}$$

$$\rho=q\left(\sum_{k=1}^{N}z_k n_k-n_e\right) \tag{2}$$

where, ε_0 is the relative dielectric constant of air. ε_r is the relative dielectric constant of the medium, and V is the potential. ρ is the charge of a node in space. n_e is the electron number density. q is the charge amount of the basic point charge ($1.602e^{-19}$ C). z_k represents the number density of particles of a certain substance within a unit volume. It is used to denote the number of particles present in a specified volume. n_k is the number of electrons lost by these particles, indicating the number of electrons each particle has lost due to ionization. In an un-ionized state, a particle is typically electrically neutral, meaning that the number of positive charges (determined by the number of protons in the nucleus) is equal to the number of negative charges (determined by the number of electrons surrounding the nucleus). When a particle loses electrons, it becomes a positively charged ion. For each electron lost, an additional unit of positive charge is acquired. Therefore, if a particle loses n_k electrons, it will carry n_k units of positive charge.

2) DRIFT-DIFFUSION AND CHEMICAL REACTIONS

The electron transport equation quantitatively characterizes the evolution of the electron number density and the electron energy density within plasma during reactive processes. The equations are as following equations (3) and (4):

$$\frac{\partial n_{\mathrm{e}}}{\partial t} + \nabla \cdot \boldsymbol{\Gamma}_{\mathbf{e}} = R_{\mathrm{e}} - (\boldsymbol{u} \cdot \nabla) n_{\mathrm{e}} \tag{3}$$

$$\frac{\partial n_{\varepsilon}}{\partial t} + \nabla \cdot \boldsymbol{\Gamma}_{\boldsymbol{\varepsilon}} + \boldsymbol{E} \cdot \boldsymbol{\Gamma}_{\mathbf{e}} = R_{\boldsymbol{\varepsilon}} - (\boldsymbol{u} \cdot \nabla) n_{\boldsymbol{\varepsilon}} \tag{4}$$

n_{ε} is the electron energy density. R_{e} is the electron source term, representing the number of electrons generated per unit time within a unit volume of the plasma. $\boldsymbol{u}$ is the macroscopic convection velocity of the neutral background gas. The calculation formula of R_{e} is as following equation (5):

$$R_{\mathrm{e}} = \sum_{j=1}^{\mathrm{M}} x_j \alpha_j N_{\mathrm{n}} \left| \boldsymbol{\Gamma}_{\mathbf{e}} \right| \tag{5}$$

wherein, x_j is the Mole fraction of the target substance of reaction j. α_j is Townsend coefficient of reaction j, which describes the probability of gas ionization per unit path length by an electron under the influence of an electric field for reaction j. N_{n} is the total density of neutral particles.

$\boldsymbol{\Gamma}_{\mathbf{e}}$ is the electron flux. The calculation formulas are as following equations (6) (7):

$$\boldsymbol{\Gamma}_{\mathbf{e}} = -(\mu_{\mathrm{e}} \cdot \boldsymbol{E}) n_{\mathrm{e}} - \nabla (D_{\mathrm{e}} n_{\mathrm{e}}) \tag{6}$$

$$\boldsymbol{\Gamma}_{\boldsymbol{\varepsilon}} = -(\mu_{\varepsilon} \cdot \boldsymbol{E}) n_{\boldsymbol{\varepsilon}} - \nabla (D_{\varepsilon} n_{\boldsymbol{\varepsilon}}) \tag{7}$$

μ_{e} is electron mobility. D_{e} is the electron diffusion coefficient. μ_{ε} is the electron energy density mobility. D_{ε} is the electron energy density diffusion coefficient. The relationship between D_{e}, μ_{ε}, D_{ε} satisfies Einstein relationship, as following equations (8), (9), and (10):

$$D_{\mathrm{e}} = \mu_{\mathrm{e}} T_{\mathrm{e}} \tag{8}$$

$$\mu_{\varepsilon} = \frac{5}{3} \mu_{\mathrm{e}} \tag{9}$$

$$D_{\varepsilon} = \mu_{\varepsilon} T_{\mathrm{e}} \tag{10}$$

In this study, μ_{e} was used to determine D_{e}, μ_{ε} and D_{ε}. The calculation formulas of electronic temperature and the average electron energy are as the following equations (11) and (12):

$$T_{\mathrm{e}} = \frac{2}{3} \bar{\varepsilon} \tag{11}$$

$$\bar{\varepsilon} = \frac{n_{\varepsilon}}{n_{\mathrm{e}}} \tag{12}$$

The dependency of electron energy density on the electric field strength is pronounced in the context of the high-pressure atmospheric conditions of the simulation. This relationship permits the utilization of a local field approximation approach to compute the electron energy density.

In plasma chemical processes, the reactants are subject to the principle of conservation of mass. The mass conservation equation for each species involved in the reaction (13) is articulated as following:

$$\rho \frac{\partial}{\partial t}(w_k) + \rho \left(\boldsymbol{u} \cdot \nabla \right) w_k = \nabla \cdot \boldsymbol{j_k} + R_k \tag{13}$$

ρ is the density of the mixture. w_k is the mass fraction. R_k is the reaction rate expression of species k.

The diffusive flux $\boldsymbol{j_k}$ is typically defined as the mass of species k passing through a unit area per unit time due to diffusion, and it is directly proportional to the diffusion velocity $\boldsymbol{V_k}$ under the assumption that the molar mass of the species remains constant. The relationship can be expressed as equation (14):

$$\boldsymbol{j_k} = \rho w_k \boldsymbol{V_k} \tag{14}$$

According to the law of conservation of mass, w_k should satisfy the equation (15):

$$\sum\nolimits_k w_k = 1 \tag{15}$$

In practical scenarios, the spatial distribution of mixtures can exhibit a high degree of complexity. Attempting to account for all the detailed local variations can render the calculation process extremely complex and analytically intractable. Therefore, to simplify the problem and make it solvable, research often resorts to using the average values of mixtures because their effects on overall macro characteristics tend to cancel each other out. To simplify the problem and make it solvable, this study resorts to using the average values of mixtures allowing for an effective description and prediction of the macroscopic behavior of the entire system without sacrificing significant accuracy.

The numerical value of $\boldsymbol{V_k}$ can be expressed by the following equation (16):

$$\boldsymbol{V_k} = D_{k,\mathrm{m}} \frac{\nabla w_k}{w_k} + D_{k,\mathrm{m}} \frac{\nabla M_{\mathrm{m}}}{M_{\mathrm{m}}} + D_k^{\mathrm{T}} \frac{\nabla T}{T} - z_k \mu_{k,\mathrm{m}} \boldsymbol{E} \tag{16}$$

$D_{k_{,\mathrm{m}}}$ typically represents the diffusion coefficient of substance k. M_{m} denotes the average molar mass of the mixture, and T signifies the system temperature (300 K). D_k^{T} is the thermal diffusion coefficient for the k^{th} species, while z_k indicates the number of charges carried by substance k. $\mu_{k_{,\mathrm{m}}}$ refers to the mobility of substance k within the mixture. Since the plasma in this experiment is in a cold state with a nearly uniform temperature distribution, the effects of thermal diffusion can be disregarded and D_k^{T} is therefore set to 0. In the simulation model developed for this paper, w_{k} is selected as the buffer gas (Air). The density of the mixture, ρ, is determined using Equation (17):

$$\rho = M_m \frac{p_{\mathrm{A}}}{RT} \tag{17}$$

R represents the ideal gas constant (8.314 J/(mol·K)), and p_{A} denotes the absolute pressure, which in this context corresponds to the background gas at atmospheric pressure of 1 atm.

The diffusion coefficient $D_{k,\mathrm{m}}$ is calculated according to Equation (18):

$$D_{k,\mathrm{m}} = 2.66 \cdot 10^{-2} \cdot \frac{\sqrt{T^3(M_k + M_m)/(2 \cdot 10^3 M_k M_m)}}{p_{\mathrm{A}} \sigma_k \sigma_m \mu_{\mathrm{X}}} \tag{18}$$

where, M_k and M_m are the molar masses of substances k and m respectively, σ_k and σ_m are the potential characteristic lengths for substances k and m respectively, and μ_{X} represents the dipole moment of substance X. These relevant parameters and variables must be determined as prerequisite conditions for the calculations prior to solving the model.

Assuming that there are Q reactions producing substance k, then the reaction rate expression for substance ψ_{k} is given by Equation (19):

$$\psi_k = \lambda_n^k \prod_{n=c}^{Q} c_n^{v_n} \tag{19}$$

In the context, λ_n^k represents the reaction rate constant for the n^{th} reaction forming substance k, c_n denotes the concentration of the n^{th} reactant, v_n signifies the order of the n^{th} reaction with respect to the formation of substance $k$and Qindicates the total number of reactions contributing to the formation of substance k.

Due to the plasma being in a cold state for the simulation study, the impact of elastic collisions on gas pressure and temperature is disregarded. Consequently, the research focuses primarily on three types of reactions: inelastic collisions, ionizing collisions, and excitation collisions.

The reaction rate constant for inelastic collisions is denoted by λ and has been established within the study. This is attributed to the fact that corona discharges are predominantly driven by the acceleration and collision processes of electrons and due to the greater mass of heavy particles, they generally attain lesser acceleration and consequently gain minimal energy from collisions. During corona discharge events, collisions among heavy particles are typically considered thermal collisions, implying that their relative velocities are close to a thermal equilibrium velocity distribution. Hence, in addressing the reactions of heavy particles within corona discharges, it can be assumed that the inelastic collision cross-section remains constant. This assumption simplifies the calculations while still providing a reasonable depiction of the system's behavior.

Ionizing collisions and excitation collisions involve the microscopic mechanisms of interactions between electrons and heavy particles. During local discharge processes, the kinetic energy of electrons is significantly influenced by the electric field. Therefore, to accurately calculate their reaction rates, it is essential to consider the collision cross-section. The determination of the reaction rate, represented by λ, entails convolving the collision cross-section with the Electron Energy Distribution Function (EEDF). As it is contingent on the electron temperature (T_{e}), this relationship is articulated in Equation (20).

$$\lambda\left(T_{\mathrm{e}}\right) = \int_0^{\infty} EEDF\left(\varepsilon\right) \cdot \sigma\left(\varepsilon\right) \cdot v\left(\varepsilon\right) d\varepsilon \tag{20}$$

$\sigma(\varepsilon)$ represents the imported collision cross-section data. The expression for electron velocity, $v(\varepsilon)$, is provided in Equation (21):

$$v\left(\varepsilon\right) = \sqrt{\frac{2\varepsilon}{m_{\mathrm{e}}}} \tag{21}$$

m_{e} denotes the mass of an electron, which is (9.1×10^{-31} kg).

In this study, measurements and analyses of the spectral characteristics of local discharges were conducted, from which the main excitation reactions occurring during the partial discharge process were deduced. Moreover, a review of the relevant literature was undertaken to obtain data on the collision cross-sections associated with these reactions.

For the simulation of the partial discharge phenomena, a total of 26 collision cross-sections were incorporated. This included 23 fundamental reactions related to gas emissions, as identified by S. Pancheshnyi et al., and an additional three major excitation reactions during the corona discharge phase, which were ascertained through spectral analysis of discharge experiments, the details of these reactions, along with other physical parameters, are presented across Tables 1, 2 and 3 [58], [59], [60], [61], [62], [63], [64], [65], [66].

TABLE 1. [58], [59], [60], [61], [62], [63], [64], [65], [66] Reactant parameters incorporated in the simulation.

substance	Molar mass (kg/mol)	Characteristic potential length (angstrom)	Minimum potential energy (K)
e			
N_2	0.02801	3.621	97.53
N_2+	0.02801	3.621	97.53
N_4+	0.5602	4.371	197.53
O_2	0.032	3.458	107.4
O_3	0.048	4.002	400
O	0.016	2.750	80
O_2+	0.032	3.458	107.4
O_4+	0.064	4,732	525
N_2O_2+	0.06002	4.621	150.53
O_2-	0.032	3.458	107.4
O-	0.016	2.750	80
N_2 $a^1\Pi_g$	0.02801	3.621	97.53
N_2 $C^3\Pi_u$	0.02801	3.621	97.53
N_2 $c_4'\Sigma_u^+$	0.02801	3.621	97.53

3) BOUNDARY CONDITIONS AND MODELING

In this simulation, a 2.5D axisymmetric model was implemented, incorporating several boundary conditions tailored to the specific physical scenario. The axis of symmetry is governed by axisymmetric boundary conditions, ensuring that physical quantities exhibit rotational symmetry about this axis. Insulating boundaries are applied where no charge

TABLE 2. [58], [59], [60], [61], [62], [63], [64], [65], [66] **Units for magnetic properties.**

react equation	Quantity	Δ(eV)
N_2+e=>2e+N_2^+	ionization	15.4
N_2^++e+N_2=>2N_2	Attach	
N_2^++2e=>N_2+e	Attach	
O_2+e=>2e+O_2^+	ionization	
O_4^++e=>2O_2	Attach	
O_2^++e=>2O	Attach	
2O_2+e=>O_2+O_2^-	Attach	
N_2^++N_2+O_2=>N_4^++O_2	mass transfer	
N_2^++N_2+N_2=>N_4^++N_2	mass transfer	
N_4^++ O_2=>O_2^++2N_2	mass transfer	
N_2^++ O_2=>O_2^++N_2	mass transfer	
2N_2^++ O_2^+=>$N_2O_2^+$+N_2	mass transfer	
$N_2O_2^+$+ O_2=>O_4^++N_2	mass transfer	
O_2^++ O_2+ O_2=>O_4^++ O_2	mass transfer	
O_2^++ O_2+ N_2=>O_4^++ N_2	mass transfer	
O_4^++ O_2^- =>3O_2	mass transfer	
O_4^++ O_2^-+ O_2=>3O_2+ O_2	mass transfer	
O_4^++ O_2^-+ N_2=>3O_2+ N_2	mass transfer	
O_2^++ O_2^-+ O_2=>2O_2+ O_2	mass transfer	
O_2^++ O_2^-+ N_2=>2O_2+ N_2	mass transfer	
O+ O_2+ N_2=>O_3+ N_2	mass transfer	
O+ O_2+ O_2=>O_3+ O_2	mass transfer	
N_2: $X^1\Sigma_g^+$+e= e+N_2: $a^1\Pi_g$	Excitation	9.191
N_2: $X^1\Sigma_g^+$+e= e+N_2: $C^3\Pi_u$	Excitation	11.03
N_2: $X^1\Sigma_g^+$+e= e+N_2: $c_4'^1\Sigma_u^+$	Excitation	12.935

TABLE 3. [58], [59], [60], [61], [62], [63], [64], [65], [66] **Table of secondary electron emission characteristics.**

Equation	Secondary emission coefficient	The average energy of the secondary electron
N^+=>N	0.02	5
N_4^+=>2N_2	0.02	5
O_2^+=>O_2	0.05	2.5
O_4^+=>2O_2	0.02	2.5
$N_2O_2^+$=>N_2+O_2	0.02	3
O_2^-=>O_2	0	0
O^-=>0.5O_2	0	0
O_3=>1.5O_2	0	0
O=>0.5O_2	0	0

transfer is expected, effectively treating the external air boundaries as non-conductive, this can be expressed by the following formula (22), (23):

$$-\mathbf{n}\cdot\boldsymbol{\Gamma}\mathbf{e}=0 \tag{22}$$

$$-\mathbf{n}\cdot\boldsymbol{\Gamma}\boldsymbol{\varepsilon}=0 \tag{23}$$

The model distinguishes between grounding and metallic contact for wall boundaries:

Metallic contacts are modeled with constant potential boundaries to simulate perfect electrical conductivity can be expressed by the following formulas (24), (25):

$$V=V_0-I_pR_b-R_bC_b\frac{dV}{dt} \tag{24}$$

$$I_p=\int_{\partial\Omega}(\mathbf{n}\cdot\boldsymbol{J}_\mathbf{i}+\mathbf{n}\cdot\boldsymbol{J}_\mathbf{e}+\mathbf{n}\cdot\boldsymbol{J}_\mathbf{d})dS \tag{25}$$

V represents the surface voltage, V_0 is the initial voltage, I_p denotes the total current passing through the closed surface $\partial\Omega$, R_b corresponds to the virtual resistance of the simulation circuit, C_b is the virtual capacitance of the simulation circuit, $\boldsymbol{J}_\mathbf{i}$ refers to the ion current density, $\boldsymbol{J}_\mathbf{e}$ is the electron current density, and $\boldsymbol{J}_\mathbf{d}$ signifies the displacement current density.

While grounding conditions are assigned to specific surfaces, serving as reference points for zero electric potential, can be expressed by the following formula (26):

$$V=0 \tag{26}$$

As boundary conditions for the plasma wall interface, the following flux boundary conditions for electron density and electron energy density on the reactive wall are given as formulas (27), (28):

$$\mathbf{n}\cdot\boldsymbol{\Gamma}\mathbf{e}=\frac{1-r}{1+r}\left(\frac{1}{2}\bar{\boldsymbol{v}}_{\mathbf{e,th}}\right)\boldsymbol{\iota}_\mathbf{e}-[\Sigma_i z_i\psi_i\boldsymbol{\Gamma}_i\cdot\mathbf{n}+\mathbf{n}\cdot\boldsymbol{\Gamma}_t] \tag{27}$$

$$\mathbf{n}\cdot\boldsymbol{\Gamma}\boldsymbol{\varepsilon}=\frac{1-r}{1+r}\left(\frac{5}{6}\bar{\boldsymbol{v}}_{\mathbf{e,th}}\right)\boldsymbol{\zeta}_\varepsilon-[\Sigma_i\varepsilon_i\psi_i\boldsymbol{\Gamma}_i\cdot\mathbf{n}+\bar{\varepsilon}(\mathbf{n}\cdot\boldsymbol{\Gamma}_t)] \tag{28}$$

In the research of a cold state plasma, it can be assumed throughout the calculation process that both the thermal emission flux, denoted by $\boldsymbol{\Gamma}_\mathbf{t}$, and the average energy of thermal ions, represented by $\bar{\varepsilon}$, are zero. $\mathbf{n}$ is the vector normal to the wall, and $\bar{\boldsymbol{v}}_{\mathbf{e,th}}$ is the thermal velocity of electrons, the value is related to the electron temperature. In this study, $\bar{\boldsymbol{v}}_{\mathbf{e,th}}$ can be calculated using the following Equation (29):

$$\bar{\boldsymbol{v}}_{\mathbf{e,th}}=\sqrt{\frac{2k_BT_e}{m_e}}\cdot\mathbf{n} \tag{29}$$

$\boldsymbol{\iota}_\mathbf{e}$ represents the normal electron flux density, $\boldsymbol{\zeta}_\boldsymbol{\varepsilon}$ denotes the normal energy flux density, and $\boldsymbol{\zeta}_\boldsymbol{\varepsilon}$ is determined by Equation (30):

$$\boldsymbol{\zeta}_\boldsymbol{\varepsilon}=\frac{3}{2}\boldsymbol{\iota}_e k_BT_e=\frac{3}{2}n_e k_BT_e\cdot\mathbf{n} \tag{30}$$

z_i corresponds to the number of electrons lost in the i^{th} type of reaction, ε_i represents the energy lost in the i^{th} type of reaction, $\boldsymbol{\Gamma}_\mathbf{i}$ denotes the incident flux of the i^{th} class of particles, and $\sum_i z_i\psi_i\boldsymbol{\Gamma}_\mathbf{i}\cdot\mathbf{n}$ and $\sum_i\varepsilon_i\psi_i\boldsymbol{\Gamma}_\mathbf{i}\cdot\mathbf{n}$ pertain to the total secondary electron emission flux and secondary electron energy flux density, respectively, for surface reaction i. ψ_i is determined via Equations (31) and (32):

$$\psi_i=\lambda_l^f\prod_{n=1}^{Q}c_n^{v_n} \tag{31}$$

$$\lambda_l^f=\frac{1}{4}\sqrt{\frac{8RT}{\pi M_w}}\left(\frac{\gamma_l}{1-\gamma_l/2}\right)\prod_{k=\text{surf}}\left(\frac{\sigma_k}{\Gamma_{\text{tot}}}\right)^{v_{kl}^f} \tag{32}$$

Referencing the reaction rate calculation method described in this paper, ψ_i represents the total reaction rate for

the l^{th} type of reaction. M_w is as previously described, corresponding to the molar mass of the w^{th} type of molecule. Continuing as before, R denotes the ideal gas constant, and T is the temperature. σ signifies the characteristic length of the electric potential for particles, Γ_{tot} is the total surface site concentration, representing the total number of active sites per unit surface area. Prior to the commencement of the simulation, the values for σ and Γ_{tot} serve as inputs within the simulation parameters.

The simulation employed the finite element method (FEM) to establish a 2.5D axisymmetric model. 2.5D model is an extension of the 2D model, is commonly used to describe cylindrical or annular electrode systems in electrical discharge studies, accurately describes the distribution of electric, magnetic, and other physical quantities depending on the distance from the axis of symmetry, particularly useful for analyzing discharge phenomena in axisymmetric electrode structures while maintaining computational efficiency. For plasma models that take into account the collision cross-sections of chemical reactions, the complexity of solving 3D models is extremely excessive. Direct computation using three-dimensional models almost fails to converge. The 2.5D axisymmetric model provides an effective and accurate solution. Additionally, to prevent the point structure of the simulation model from affecting the development of the discharge and the convergence of the simulation, the model is constructed using continuous curves without altering the curvature of the electrode tip. The structure of the model and the division of the mesh are illustrated in Figure 9:

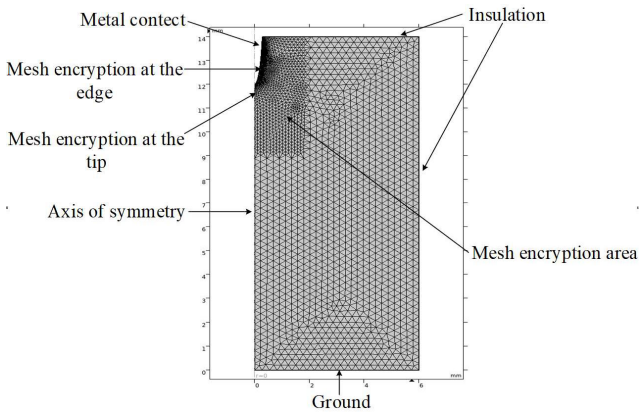

FIGURE 9. 2.5D Axisymmetric simulation model of needle-plate electrode discharge.

B. B SIMULATION RESULT AND ANALYSIS

The transient distribution of micro-particles during discharge obtained through simulation is shown in Figures 10, 11, and 12. Figures 10 and 11 do not incorporate the excitation transition of N2 from the ground state to the neutral excited-state. Correspond to electrode voltages of −3 kV and −3.5 kV, respectively. Figure 12 corresponds to an applied voltage of −3.5 kV and takes into account 23 types of atmospheric reactions as well as the discharge electron

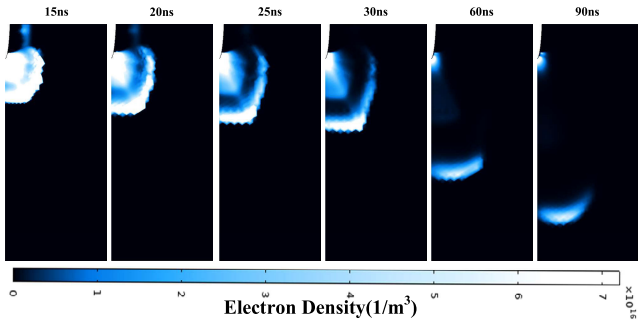

FIGURE 10. Electron density during discharge under the applied voltage of −3.0 kV (Excluding the Neutral Excitation Transition of N_2).

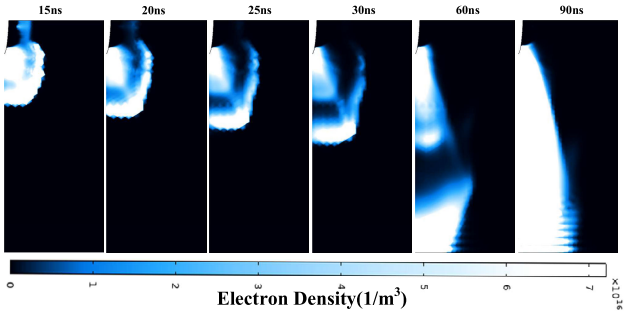

FIGURE 11. Electron density during discharge under the applied voltage of −3.5 kV (Excluding the Neutral Excitation Transition of N_2).

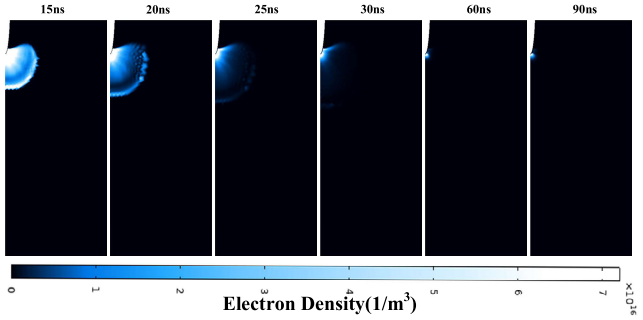

FIGURE 12. Electron density during discharge under the applied voltage of −3.5 kV (Incorporating the Neutral Excitation Transition of N_2).

density distribution incorporating the N_2 ground state to neutral excited-states level transition reaction.

Visualizing the process of electron density in plasma discharges is challenging due to the wide range of electron densities. Very high densities are shown as bright white on the chart, while low densities are represented as black. Without a set display threshold, the image would be predominantly black, making it difficult to examine the critical discharge processes leading to electrical breakdown. Moreover, setting the display to an exponential mode would make the image incomprehensible.

Therefore, the maximum value of electron density displayed in images is capped at 7.2×10^{16} (any region exceeding this value is displayed as white), the actual electron density may reach as high as 2×10^{18}. This display limitation aids in focusing on the crucial stages of plasma discharge. Research indicates that when the electron density in the channel formed

at the gap between the two ends exceeds 7.2×10^{16}. This is a significant increase in current can be observed, indicative of the formation of a conductive channel, which will leading to a rapid transition of the local discharge into the breakdown phase.

Setting this display threshold makes it possible to clearly observe the formation and development of the conductive channel in the images. This visualization approach facilitates more precise tracking and analysis of the key discharge processes that lead to breakdown.

Transient electron density distribution charts vividly depict the evolution trend of electron density during the discharge process. At the instant the applied voltage impacts the gap, a pulse swiftly forms, leading to two high-density electron regions within the discharge area: a region of free electrons evolving at the discharge periphery, and an internal region characterized by a corona discharge resulting from electron breakdown.

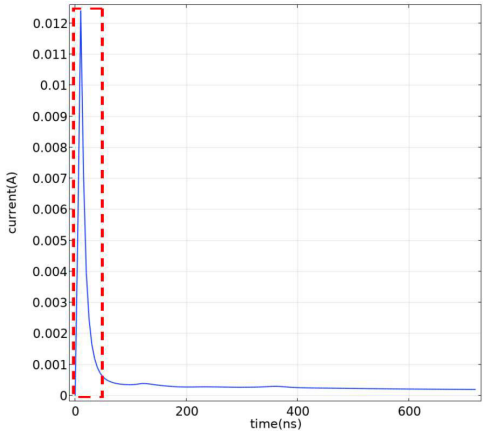

FIGURE 13. Discharge current over time under the applied voltage of −3.0 kV (Excluding the Neutral Excitation Transition of N_2).

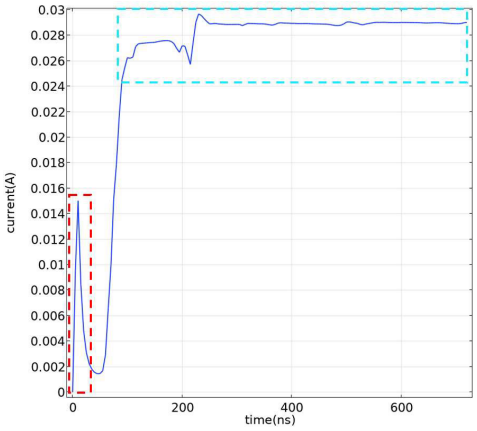

FIGURE 14. Discharge current over time under the applied voltage of −3.5 kV (Excluding the Neutral Excitation Transition of N_2).

As shown in Figures 13, 14, and 15. By correlating the transient electron density distribution with current variation charts, an initial current peak is noticed in all three states, The

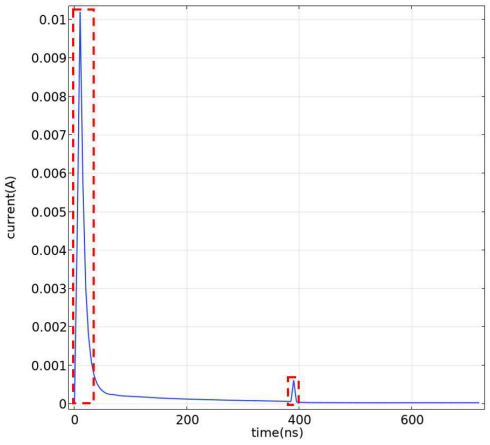

FIGURE 15. Discharge current over time under the applied voltage of −3.5 kV (Incorporating the Neutral Excitation Transition of N_2).

current characteristic is similar to the Trichel pulses observed in negative corona discharges. As depicted in Figure 13, in the model excluding the neutral excitation transition of N_2 ground-state molecules with an applied voltage of −3 kV, a current peak emerges due to the generation of electron avalanche event. Following the propagation of the free-electron pulse to the alternate electrode, the current undergoes a rapid decrease. However, the non-zero current value indicates an ongoing discharge in the gap. This can be attributed to the formation of a conductive channel due to continuous electron collisions, providing conductivity to the gap, albeit with substantial resistance. Therefore, the gap maintains a weak self-sustained discharge state.

As depicted in Figure 15, with an applied voltage of −3.5 kV, a conductive channel rapidly forms as the free-electron pulse propagates to the opposite pole and will ultimately result in gap breakdown. Consequently, the current exhibits a trend of initial decrease followed by a rapid breakdown.

In the model that incorporates the excitation transition of N2 from the ground state to the neutral excited-state, the free-electron pulse begins to diminish after reaching the opposite pole, causing a swift decline in current. Accompanying the current decrease, the conductive channel gradually fades away, after that the electric charge at both ends of the gaps will accumulate repeatedly, and then the subsequent discharge pulse forms again around the 400 ns mark in the figure.

As shown in Figures 16 and 17, electron density evolution on the central axis reflects the development of electron avalanche. As the figures depicted starting from the high-voltage end and extending to the end of the streamer, an electron avalanche exists, in the head of the electron avalanche the electron density peaks and then rapidly decreases. At this point, the free-electron pulse is constituted by the field emitted electron and the free electrons generated due to electron avalanche. If a substantial number of free electrons are generated from electron avalanche, the electron density curve exhibits a more gradual decline.

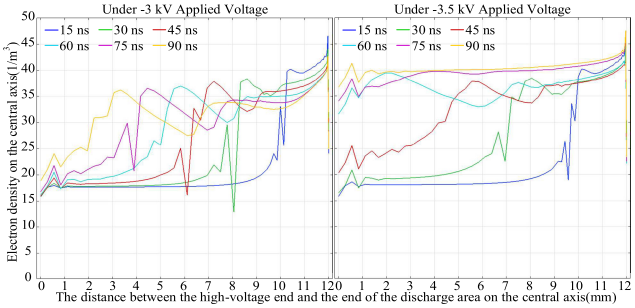

FIGURE 16. Comparison of electron density evolution on the central axis during discharge under the applied voltages of −3.0 kV and −3.5 kV (Excluding the Neutral Excitation Transitions of N_2).

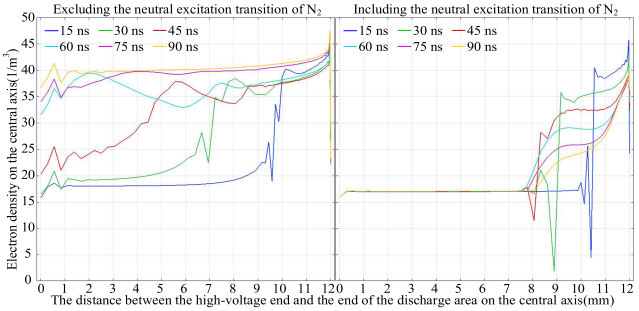

FIGURE 17. Comparison of electron density evolution on the central axis during discharge under the applied voltage of −3.5 kV, with and without incorporation of the neutral excitation transitions of N_2.

Although there isn't a significant difference in electron density among the initial electron avalanches generated by the free-electron pulse under −3.5 kV voltage, the electron avalanche propagation speed is noticeably higher than that under −3.0 kV voltage. When the stream extends to half of the gap, electron energy of the head of the electron avalanche can still high enough to sustain further electron avalanche reactions. After the electron pulse reaches the other electrode, the gas molecules in the gap undergo ionization to form a conductive channel, resulting in breakdown.

Under the applied voltage of −3.0 kV, although the electron avalanche can still advancing, the electron density within the potential breakdown channel is significantly reduced, resulting in a lower degree of ionization. Makes it unpossible to maintain a conductive channel. Therefore, when the pulse reaches the cathode, breakdown does not occur.

As depicted in the figures under the influence of −3.5 kV voltage, when incorporating the excitation reactions caused by N_2 from the ground state to the neutral excited-state, the electron density at the head of the electron avalanche is truncated. This is because the reactions involving from the ground state to the excited state take advantage of the competition with ionization reactions. While these reactions consume a significant amount of electron energy, they do not directly produce free electrons or ionization channels. Consequently, the development of the electron avalanche is effectively limited.

IV. CONCLUSION

This study investigates the interaction and impact of free-electron pulse and neutral excited-state species formation during the negative corona discharge process. Simulation reveals that free-electron pulse significantly promotes the development of discharge and the formation of breakdown, while the generation of neutral excited-state species results in electron energy loss, hindering further collision reactions caused by free-electron pulse that would produce high-energy electrons, thus acting as an inhibiting factor in breakdown formation. During the discharge process, free-electron pulse not only facilitates the development of corona discharge and breakdown formation but also accompanies intense excitation reactions. Despite their short duration, they have a substantial influence on discharge development.

The conclusion enriches our understanding of corona discharge processes and further reveals the influence of free-electron pulse and the formation of neutral excited state species on this process. This may provide meaningful theoretical references for optimizing the design of electrical equipment and improving equipment operational efficiency.

V. FUTURE RESEARCH DIRECTIONS

Building on the insights from this study, the research concludes two methods for improving the properties of the electrical equipment:

A. DESIGN OF GAS COMPOSITION IN INTERNAL INSULATING SYSTEMS

The application of the internal insulating electrical equipment is becoming more and more widespread in the future. Due to the outstanding insulating properties and chemical stability, SF6 still remains the most effective gas insulation medium. However, it is also a gas with a potent greenhouse effect. Thus finding an environmentally friendly alternative gas is an important research direction. Previous research has mainly focused on large molecular gases, attempting to use their adsorption of free electrons to eliminate the free electrons produced by discharge. However, large molecular gas media generally have the following defects: they have a large molecular mass and are prone to liquefy in low-temperature environments, especially in sealed composite electrical equipment with internal insulation that requires pressurization to enhance insulation performance, significantly limiting their scope of use; Additionally, large molecular gases typically have complex molecular structures, which may make them more susceptible to decomposition in high-energy discharge environments. The decomposition of the gas medium leads to a continuous decline in its insulating properties. Moreover, the decomposition products may be harmful and could damage the performance of electrical equipment; Furthermore, the synthesis and purification process of large molecular gases may be more complex, involving multiple steps of chemical reactions, resulting in higher costs for preparing large molecular gases. This research proposes another approach to designing insulating

gases, by consuming the energy of free electrons through excitation reactions. The integration of specific buffer gases into the composition of gases within internal insulating systems is proposed to facilitate the generation of certain excited neutral species. This alteration is theorized to affect the energy distribution during electron collisions, thereby reducing the risk of electrical breakdown.

B. APPLY SPECIALIZED ELECTRODES' SURFACE COATINGS

It is recommended to apply specialized coating materials with strong electron binding capabilities on the surfaces of electrodes. This helps in reducing the initial electron temperature of free electrons formed by field emission during the onset of discharge pulses and also lowers the secondary electron emission coefficient. By doing this, the electron avalanche effect can be mitigated. Moreover, some coatings may absorb a portion of the discharge energy and transform it into less harmful forms, such as heat or light, thus reducing the total energy released during discharge. Additionally, the physical properties of coating materials may influence the rate of generation of excited neutral species, thereby expediting the energy loss of electrons.

Although theoretically neutral excited-state molecules bear a close structural resemblance to their ground-state counterparts, their presence could subtly influence the discharge process. The genesis of neutral excited-state species may initiate a series of subsequent reactions, for instance, generating novel free radicals or other reactive intermediates such as certain metastable entities through collision-induced de-excitation. These species could incrementally build up, altering the dynamics of discharge channel formation and evolution, thereby affecting the characteristics of the PD. Nevertheless, due to the relatively low energy involved in local discharges, the quantity of neutral excited-state particles produced is expected to be minimal, thereby the impact of these processes on PD development might be marginal. Further research is warranted to elucidate the interplay of these phenomena across an expanded spectrum of environmental and engineering environments.

ACKNOWLEDGMENT

The authors thank the Northeastern Electric Power Research Institute, China Electric Power Research Institute, CAS Electrical Engineering Research Institute, Ocean Optics Company, and Advantis Company for their support of their research.

REFERENCES

[1] N. Baghelkar and A. Dubey, "A review of study and analysis of partial discharge for different insulation materials with capacitance value," *Int. J. Eng. Technol. Manage. Res.*, vol. 7, no. 12, pp. 64–66, Jan. 2021.
[2] J. D. S. Cruz, F. Fruett, R. D. R. Lopes, F. L. Takaki, C. D. A. Tambascia, E. R. D. Lima, and M. Giesbrecht, "Partial discharges monitoring for electric machines diagnosis: A review," *Energies*, vol. 15, no. 21, p. 7966, Oct. 2022.
[3] M. Florkowski, "Anomaly detection, trend evolution, and feature extraction in partial discharge patterns," *Energies*, vol. 14, no. 13, p. 3886, Jun. 2021.
[4] M. R. Hussain, S. S. Refaat, and H. Abu-Rub, "Overview and partial discharge analysis of power transformers: A literature review," *IEEE Access*, vol. 9, pp. 64587–64605, 2021.
[5] N. Rosle, N. A. Muhamad, M. N. K. H. Rohani, and M. K. M. Jamil, "Partial discharges classification methods in XLPE cable: A review," *IEEE Access*, vol. 9, pp. 133258–133273, 2021.
[6] S. Zhang, C. Li, K. Wang, J. Li, R. Liao, T. Zhou, and Y. Zhang, "Improving recognition accuracy of partial discharge patterns by image-oriented feature extraction and selection technique," *IEEE Trans. Dielectr. Electr. Insul.*, vol. 23, no. 2, pp. 1076–1087, Apr. 2016.
[7] M. Ren, B. Song, T. Zhuang, and S. Yang, "Optical partial discharge diagnostic in SF6 gas insulated system via multi-spectral detection," *ISA Trans.*, vol. 75, pp. 247–257, Apr. 2018.
[8] J. M. Rodríguez-Serna and R. Albarracín-Sánchez, "A study on the life estimation and cavity surface degradation due to partial discharges in spherical cavities within solid polymeric dielectrics using a simulation based approach," *Polymers*, vol. 13, no. 3, p. 324, Jan. 2021.
[9] Y. Zang, Y. Qian, H. Wang, A. Xu, G. Sheng, and X. Jiang, "Method of GIL partial discharge localization based on natural neighbour interpolation and ECOC-MLP-SVM using optical simulation technology," *High Voltage*, vol. 6, no. 3, pp. 514–524, Jun. 2021.
[10] M. Azizian Fard, M. E. Farrag, A. Reid, and F. Al-Naemi, "Electrical treeing in power cable insulation under harmonics superimposed on unfiltered HVDC voltages," *Energies*, vol. 12, no. 16, p. 3113, Aug. 2019.
[11] B. Luo, J. Wang, D. Dai, L. Jia, L. Li, and T. Wang, "Partial discharge simulation of air gap defects in oil-paper insulation paperboard of converter transformer under different ratios of AC–DC combined voltage," *Energies*, vol. 14, no. 21, p. 6995, Oct. 2021.
[12] G. C. Montanari, "Aging and life models for insulation systems based on PD detection," *IEEE Trans. Dielectr. Electr. Insul.*, vol. 2, no. 4, pp. 667–675, 1995.
[13] A. M. Loveless, A. M. Darr, and A. L. Garner, "Linkage of electron emission and breakdown mechanism theories from quantum scales to Paschen's law," *Phys. Plasmas*, vol. 28, no. 4, pp. 042110-1–042110-13, Apr. 2021.
[14] R. Sasamoto, T. Matsumoto, H. Orii, Y. Izawa, and K. Nishijima, "Quantitative visualization of gas temperature distribution in atmospheric DC glow corona by spectral image processing," in *Proc. IEEE Conf. Electr. Insul. Dielectric Phenomena (CEIDP)*, Oct. 2016, pp. 203–206.
[15] S. A. Shcherbanev, I. U. Nadinov, P. Auvray, S. M. Starikovskaia, S. Pancheshnyi, and L. G. Herrmann, "Emission spectroscopy of partial discharges in air-filled voids in unfilled epoxy," *IEEE Trans. Plasma Sci.*, vol. 44, no. 7, pp. 1219–1227, Jul. 2016.
[16] B. Tang, D. Han, Y. Li, K. Li, Z. Qiu, and G. Zhang, "Analysis on characteristic emission spectrum of SF6 under 50 Hz AC corona discharge," in *Proc. IEEE Electr. Insul. Conf. (EIC)*, Jun. 2021, pp. 711–714.
[17] X. Zhang, H. Liu, J. Ren, J. Li, and X. Li, "Fourier transform infrared spectroscopy quantitative analysis of SF6 partial discharge decomposition components," *Spectrochimica Acta A, Mol. Biomolecular Spectrosc.*, vol. 136, pp. 884–889, Feb. 2015.
[18] Y. Zhao, X. Wang, D. Dai, Z. Dong, and Y. Huang, "Partial discharge early-warning through ultraviolet spectroscopic detection of SO2," *Meas. Sci. Technol.*, vol. 25, no. 3, Mar. 2014, Art. no. 035002.
[19] Z.-C. Luo, F.-Y. Han, B. Tang, L.-F. Zhang, C.-Y. Liu, Q.-Q. Liang, L.-P. Zhu, and J.-M. Zhang, "Optical properties and decomposition mechanisms of SF6 at different partial discharge determined by infrared spectroscopy," *AIP Adv.*, vol. 8, no. 6, pp. 065107-1–065107-6, Jun. 2018.
[20] C. Xia, M. Ren, R. Chen, J. Yu, C. Li, Y. Chen, K. Wang, S. Wang, and M. Dong, "Multispectral optical partial discharge detection, recognition, and assessment," *IEEE Trans. Instrum. Meas.*, vol. 71, pp. 1–11, 2022.
[21] X. Guo, L. Zhang, Z. Ji, Y. Gao, Z. Wang, and N. Zhao, "Three-dimensional simulation of corona discharge in a double-needle system during a thunderstorm," *Atmosphere*, vol. 14, no. 5, p. 789, Apr. 2023.
[22] Y. Liu, Z. Li, Z. Qin, X. Li, Y. Liu, H. Huang, and F. Huang, "Research on the simulation method for HVDC continuous positive corona discharge," *IEEE Trans. Plasma Sci.*, vol. 50, no. 9, pp. 2805–2814, Sep. 2022.
[23] A. Patil, D. Patil, R. Pangarkar, and D. Patil, "Modelling and FEA analysis of partial discharge phenomena in a spherical void within solid dielectric material," in *Proc. Int. Conf. Current Trends Towards Converging Technol. (ICCTCT)*, Mar. 2018, pp. 1–4.
[24] J. M. Rodríguez-Serna, R. Albarracín-Sánchez, M. Dong, and M. Ren, "Computer simulation of partial discharges in voids inside epoxy resins using three-capacitance and analytical models," *Polymers*, vol. 12, no. 1, p. 77, Jan. 2020.

[25] J. M. Rodríguez-Serna, R. Albarracín-Sánchez, and A. A. Mas'ud, "Finite-element-analysis models for numerical simulation of partial discharges in spherical cavities within solid dielectrics: A review and a novel method," *High Voltage*, vol. 5, no. 5, pp. 556–568, Oct. 2020.

[26] Y. Zhu, C. Chen, J. Shi, and W. Shangguan, "A novel simulation method for predicting ozone generation in corona discharge region," *Chem. Eng. Sci.*, vol. 227, Dec. 2020, Art. no. 115910.

[27] M. Borghei, M. Ghassemi, J. M. Rodríguez-Serna, and R. Albarracín-Sánchez, "A finite element analysis and an improved induced charge concept for partial discharge modeling," *IEEE Trans. Power Del.*, vol. 36, no. 4, pp. 2570–2581, Aug. 2021.

[28] Y. Guan, R. S. Vaddi, A. Aliseda, and I. Novosselov, "Analytical model of electro-hydrodynamic flow in corona discharge," *Phys. Plasmas*, vol. 25, no. 8, pp. 083507-1–083507-8, Aug. 2018.

[29] Y. Guan, R. S. Vaddi, A. Aliseda, and I. Novosselov "Experimental and numerical investigation of electrohydrodynamic flow in a point-to-ring corona discharge," *Phys. Rev. Fluids*, vol. 3, no. 4, Apr. 2018, Art. no. 043701.

[30] C. Zheng, X. Zhang, Z. Yang, C. Liang, Y. Guo, Y. Wang, and X. Gao, "Numerical simulation of corona discharge and particle transport behavior with the particle space charge effect," *J. Aerosol Sci.*, vol. 118, pp. 22–33, Apr. 2018.

[31] L. Liu and M. Becerra, "An efficient model to simulate stable glow corona discharges and their transition into streamers," *J. Phys. D, Appl. Phys.*, vol. 50, no. 10, Mar. 2017, Art. no. 105204.

[32] X. Guo, Q. Zhang, and J. Zhang, "Improvement of corona discharge model and its application on simulating corona discharge in the presence of wind," *Math. Problems Eng.*, vol. 2017, pp. 1–10, 2017.

[33] S. Chen, J. C. P. Y. Nobelen, and S. Nijdam, "A self-consistent model of ionic wind generation by negative corona discharges in air with experimental validation," *Plasma Sources Sci. Technol.*, vol. 26, no. 9, Aug. 2017, Art. no. 095005.

[34] Y. K. Stishkov, A. V. Samusenko, and I. A. Ashikhmin, "Corona discharge and electrogasdynamic flows in the air," *Physics-Uspekhi*, vol. 61, no. 12, pp. 1213–1226, Dec. 2018.

[35] D. Fahmi, H. A. Illias, H. Mokhlis, and I. M. Y. Negara, "Numerical investigation of negative corona discharge from protrusion on parallel plane electrodes in air insulation," *IEEE Trans. Plasma Sci.*, vol. 50, no. 10, pp. 3830–3838, Oct. 2022.

[36] Q. Gao, C. Niu, K. Adamiak, A. Yang, M. Rong, and X. Wang, "Numerical simulation of negative point-plane corona discharge mechanism in SF6 gas," *Plasma Sources Sci. Technol.*, vol. 27, no. 11, Nov. 2018, Art. no. 115001.

[37] H. Sun, S. Huang, Q. Wang, S. Wang, and W. Zhao, "Characteristics of negative corona discharge in air at various gaps," *IEEE Trans. Plasma Sci.*, vol. 47, no. 1, pp. 736–741, Jan. 2019.

[38] L. Chuan, L. Zhi, W. Pengyu, Z. Ming, Y. Yong, and Y. Kexun, "A hybrid approach for corona discharge in needle electrode configuration: In a large-scale space," *Plasma Sources Sci. Technol.*, vol. 29, no. 4, Mar. 2020, Art. no. 045011.

[39] J.-W. Zhang, C. Yin, C. Song, R.-T. Liu, and B. Li, "Numerical simulation and experiments on mono-polar negative corona discharge applied in nanocomposites," *IEEE Trans. Dielectr. Electr. Insul.*, vol. 24, no. 2, pp. 791–797, Apr. 2017.

[40] G. Callender, P. Rapisarda, and P. L. Lewin, "Improving models of partial discharge activity using simulation," in *Proc. IEEE Electr. Insul. Conf. (EIC)*, Jun. 2017, pp. 392–395.

[41] G. Callender, T. Tanmaneeprasert, and P. L. Lewin, "Simulating partial discharge activity in a cylindrical void using a model of plasma dynamics," *J. Phys. D, Appl. Phys.*, vol. 52, no. 5, Jan. 2019, Art. no. 055206.

[42] G. Callender and P. L. Lewin, "Plasma dynamic simulations of partial discharges within electrical tree structures," in *Proc. IEEE Electr. Insul. Conf. (EIC)*, Jun. 2019, pp. 340–343.

[43] G. Callender and P. L. Lewin, "Modeling partial discharge phenomena," *IEEE Elect. Insul. Mag.*, vol. 36, no. 2, pp. 29–36, Mar. 2020.

[44] A. V. Kozyrev, V. Yu. Kozhevnikov, N. S. Semeniuk, and L. A. Zyulkova, "Theoretical simulation of a gas breakdown initiated by external plasma source in the gap with combined metal–dielectric electrodes," *IEEE Trans. Plasma Sci.*, vol. 43, no. 8, pp. 2294–2298, Aug. 2015.

[45] A. Villa, R. Schurch, L. Barbieri, R. Malgesini, and G. Buccella, "An uncoupled implementation of the local mean energy plasma model," *J. Comput. Phys.*, vol. 447, Dec. 2021, Art. no. 110674.

[46] A. Villa, L. Barbieri, M. Gondola, A. R. Leon-Garzon, and R. Malgesini, "A PDE-based partial discharge simulator," *J. Comput. Phys.*, vol. 345, pp. 687–705, Sep. 2017.

[47] R. A. Leon-Garzon, G. Dotelli, M. Tommasini, C. L. Bianchi, C. Pirola, A. Villa, A. Lucotti, and A. Barbieri, "Experimental characterization of polymer surfaces subject to corona discharges in controlled atmospheres," *Polymers*, vol. 11, no. 10, p. 1646, Oct. 2019.

[48] A. Villa, G. Buccella, L. Barbieri, D. Palladini, and G. D'Avanzo, "A multi-resolution method for internal partial discharge simulation," *J. Comput. Phys.*, vol. 491, Oct. 2023, Art. no. 112362.

[49] A. Asipuela and T. Iváncsy, "Study and numerical simulation of negative and positive corona discharge: A review," *Periodica Polytechnica Electr. Eng. Comput. Sci.*, vol. 66, no. 3, pp. 294–300, Jul. 2022.

[50] X. Chen, L. Lan, H. Lu, Y. Wang, X. Wen, X. Du, and W. He, "Numerical simulation of Trichel pulses of negative DC corona discharge based on a plasma chemical model," *J. Phys. D, Appl. Phys.*, vol. 50, no. 39, Oct. 2017, Art. no. 395202.

[51] N. G. C. Ferreira, D. F. N. Santos, P. G. C. Almeida, G. V. Naidis, and M. S. Benilov, "Simulation of pre-breakdown discharges in high-pressure air. I: The model and its application to corona inception," *J. Phys. D, Appl. Phys.*, vol. 52, no. 35, Aug. 2019, Art. no. 355206.

[52] A. O. Kokovin, A. V. Kozyrev, and V. Y. Kozhevnikov, "Simulation of negative corona discharge in atmospheric air: From mode of Trichel pulses to stationary discharge," *J. Phys., Conf. Ser.*, vol. 2064, no. 1, Nov. 2021, Art. no. 012024.

[53] N. Feng, T. Ma, C. Chen, B. Yao, and W. Gao, "Simulation and study of DC corona discharge characteristics of bar-plate gap," *Energies*, vol. 15, no. 17, p. 6431, Sep. 2022.

[54] Q. T. Algwari and D. N. Saleh, "Numerical modeling of partial discharge in a void cavity within high-voltage cable insulation," *IEEE Trans. Plasma Sci.*, vol. 49, no. 5, pp. 1536–1542, May 2021.

[55] H. Timmers, X. Zhu, and Z. Li, "Disentangling conical intersection and coherent molecular dynamics in methyl bromide with attosecond transient absorption spectroscopy," *Nature Commun.*, vol. 10, no. 1, p. 3133, 2019.

[56] Y. V. Shcherbakov and R. S. Sigmond, "Subnanosecond spectral diagnostics of streamer discharges: II. Theoretical background," *J. Phys. D, Appl. Phys.*, vol. 40, no. 2, pp. 474–487, Jan. 2007.

[57] F. Valk, M. Aints, P. Paris, T. Plank, J. Maksimov, and A. Tamm, "Measurement of collisional quenching rate of nitrogen states $N_2(C^3\Pi_u, v = 0)$ and $N^+(B^2\Sigma_g^+, v = 0)$," *J. Phys. D, Appl. Phys.*, vol. 43, no. 38, Sep. 2010, Art. no. 385202.

[58] S. Pancheshnyi, M. Nudnova, and A. Starikovskii, "Development of a cathode-directed streamer discharge in air at different pressures: Experiment and comparison with direct numerical simulation," *Phys. Rev. E, Stat. Phys. Plasmas Fluids Relat. Interdiscip. Top.*, vol. 71, no. 1, Jan. 2005, Art. no. 016407.

[59] R. S. Mangina, J. M. Ajello, R. A. West, and D. Dziczek, "High-resolution electron-impact emission spectra and vibrational emission cross sections from 330–1100 nm for N_2," *Astrophysical J. Suppl. Ser.*, vol. 196, no. 1, p. 13, Sep. 2011.

[60] Y. Itikawa, "Cross sections for electron collisions with nitrogen molecules," *J. Phys. Chem. Reference Data*, vol. 35, no. 1, pp. 31–53, Mar. 2006.

[61] Y. Tohyama and T. Nagata, "Electron impact emission of N_2 2P (v', v") bands studied under single-collision condition," *J. Phys. Soc. Jpn.*, vol. 74, no. 1, pp. 326–332, 2005.

[62] C. M. Penney, R. L. S. Peters, and M. Lapp, "Absolute rotational Raman cross sections for N_2, O_2, and CO_2," *JOSA*, vol. 64, no. 5, pp. 712–716, 1974.

[63] X. Meng, B. Wu, X.-F. Gao, J.-C. Xie, H. Li, Y. Yu, D.-F. Zhao, and S. X. Tian, "Vibrationally resolved photoemissions of N_2 (C3Πu→B3Πg) and CO (b3Σ+→ a3Π) by low-energy electron impacts," *J. Chem. Phys.*, vol. 153, no. 2, pp. 024301-1–024301-8, Jul. 2020.

[64] M. J. Ajello, "Medium-resolution studies of extreme ultraviolet emission from N_2 by electron impact: Vibrational perturbations and cross sections of the C 4'Σ u+ 1 and b'Σ u+ 1 states," *Phys. Rev. A, Gen. Phys.*, vol. 40, no 7, p. 3524, 1989.

[65] C. H. Jackman, R. H. Garvey, and A. E. S. Green, "Electron impact on atmospheric gases, I. Updated cross sections," *J. Geophys. Res.*, vol. 82, no. 32, pp. 5081–5090, Nov. 1977.

[66] T. Tabata, T. Shirai, M. Sataka, and H. Kubo, "Analytic cross sections for electron impact collisions with nitrogen molecules," *At. Data Nucl. Data Tables*, vol. 92, no. 3, pp. 375–406, May 2006.

YUNING FENG received the master's degree in electrical engineering from Shenyang University of Technology, in 2019, where he is currently pursuing the Ph.D. degree. His research interests include GIS PD optical online detection based on deep learning and interpretable artificial intelligence, FEM, and FVM algorithm in the field of electrical appliances, such as MHD and PIC model, including simulation of NLTE cold plasma and LTE arc plasma.

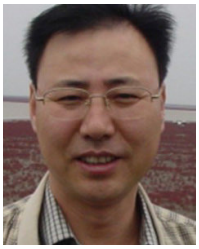

ZHIYUAN CAI received the Ph.D. degree in electrical engineering from Shenyang University of Technology, in 1987. Over the years, he has been devoted to teaching and research in the disciplines of electric machines and appliances, high voltage, and insulation technology. He has led and completed dozens of scientific research projects successfully. Proficient in solving practical engineering problems, he has obtained numerous leading research results in the fields of intelligent electrical appliances, online monitoring and fault diagnosis of high-voltage test equipment, and computer control of high-voltage experimental devices. These achievements have been widely applied across various engineering domains. He has published over 40 academic papers in significant domestic and international journals and at major international conferences, with more than 20 of them being indexed by the three major citation databases. His research interests include intelligent electrical appliances, as well as online monitoring and fault diagnosis of electrical equipment.

SHUN YUAN received the Doctor of Engineering degree in electrical machines and appliances from Xi'an Jiaotong University, in 1993. He is currently the Director of the Safety Division, China Northeast Electricity Regulatory Bureau, National Electric Power Regulatory Commission, with extensive experience in electrical engineering and power systems, and he is also a Ph.D. supervisor at the Shenyang University of Technology. His work focuses advancement of safety and regulatory standards in the power industry. He has been honored as part of the "Hundred Thousand Ten Thousand Talent Project'' in Liaoning, China, in recognition of his outstanding contributions to the fields of ultra-high voltage power transmission, insulation engineering, and electrical networks.

SHAOHUA MA received the bachelor's and Ph.D. degrees in electrical engineering from Shenyang University of Technology, in 1988 and 2008, respectively. She is currently a Professor with the School of Electrical Engineering, Shenyang University of Technology. She has successfully undertaken and completed dozens of scientific research projects. Proficient in solving practical engineering problems, she has achieved numerous leading research outcomes in the areas of intelligent electrical appliances, online monitoring and fault diagnosis of electrical equipment, and computer control of electrical equipment. These achievements have been widely applied in various engineering fields.

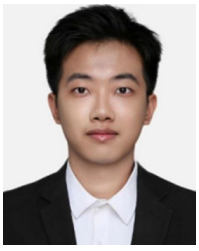

ENLIANG HUI is currently pursuing the master's degree in electrical engineering with Shenyang University of Technology. His research interests include high voltage technology, intelligent monitoring of power equipment conditions, and studies in image fusion and fault visualization.